ELSEVIER

Nuclear Instruments and Methods in Physics Research B 181 (2001) 211–218

NIM B
Beam Interactions with Materials & Atoms

www.elsevier.com/locate/nimb

Three-dimensional ion micro-tomography

A. Sakellariou, D.N. Jamieson *, G.J.F. Legge

Microanalytical Research Centre, School of Physics, The University of Melbourne, Parkville, Vic. 3010, Australia

Abstract

The technique of ion micro-tomography (IMT) provides three-dimensional distribution information about a sample's mass density and elemental composition. The required data are obtained by doing a scanning transmission ion microscopy (STIM) tomography experiment followed by a particle-induced X-ray emission (PIXE) tomography experiment. The experiment times have been vastly reduced now that data are collected with MicroDAS, the new fast data acquisition system. Moreover, the experiment is easier to perform because sample manipulation is automated via computer control. To obtain comparable spatial resolutions between the STIM and PIXE data, the PIXE tomography experiment is performed by implementing a large solid angle between the sample and X-ray detector. To correct for the inherent three-dimensional nature of such an experimental setup, a specially developed tomographic reconstruction technique is used to combine the STIM and PIXE tomography data sets to create an accurate quantitative tomogram of the sample. The efficacy of the entire IMT process is tested with a characterised ''standard'' sample. The calculated data agree well with the quantitative and structural information known about the sample. To interpret the three-dimensional distribution information, a special volume rendering program is used to visualise various aspects of the tomogram. Each aspect is colour coded to facilitate the easy visualisation of multiple complex three-dimensional structures.

PACS: 29.30.Kv; 81.70.Jb; 87.59.F
Keywords: STIM tomography; PIXE tomography

1. Introduction

The motivation for this work was to devise a technique that generates a three-dimensional distribution map of the mass density and elemental composition of micro-samples. These data can then be analysed and visualised with appropriate computer software. The mass density data are obtained with scanning transmission ion microscopy (STIM) experiments and the elemental concentration data are obtained with particle-induced X-ray emission (PIXE) experiments. However, such experiments only provide ''depth-averaged'' quantitative data. To resolve depth information, the technique of computer-assisted tomography (CAT) is used to extend the STIM and PIXE techniques. This involves collecting multiple two-dimensional STIM and PIXE scans (projections) at different angles around the sample.

* Corresponding author. Tel.: +61-3-8344-5376; fax: +61-3-9347-4783.
E-mail addresses: arthur.sakellariou@anu.edu.au (A. Sakellariou), dnj@physics.unimelb.edu.au (D.N. Jamieson).

0168-583X/01/$ - see front matter
PII: S0168-583X(01)00618-8

For the IMT experiment to be practical and the reconstructed data to be accurate, two main attributes must be optimised. The first attribute is the data acquisition time, which must be minimised. This is achieved by using a newly designed data acquisition system (DAS) [1] that can accurately collect data at very large acquisition rates. The second attribute is an accurate three-dimensional representation of the sample, to be generated by using an appropriate reconstruction algorithm. This is achieved with the the discrete image space reconstruction algorithm (DISRA) [2,3] that was developed to compensate for the many non-linear processes that occur during STIM and PIXE experiments.

Many techniques have been developed in an attempt to compensate for the non-linear processes that occur during STIM and PIXE experiments [4–15]. The main improvement over these other techniques is the ability to compensate for the effects of X-ray attenuation for a geometry in which the X-ray detector subtends a very large three-dimensional cone with the sample, as shown in Fig. 1. The purpose for such a geometry is to allow the acquisition rate of X-ray data to be sustained as the spatial resolution of the PIXE data is reduced to be comparable with the spatial resolution of the STIM data.

To demonstrate this, an experiment was done on a characterised "standard" sample. The X-ray detector was placed 12 mm from the sample at a scattering angle of 90°. With an area of 34.8 mm^2, the geometric efficiency was 0.018. At this position, the spatial resolution of the PIXE data was 0.5 μm

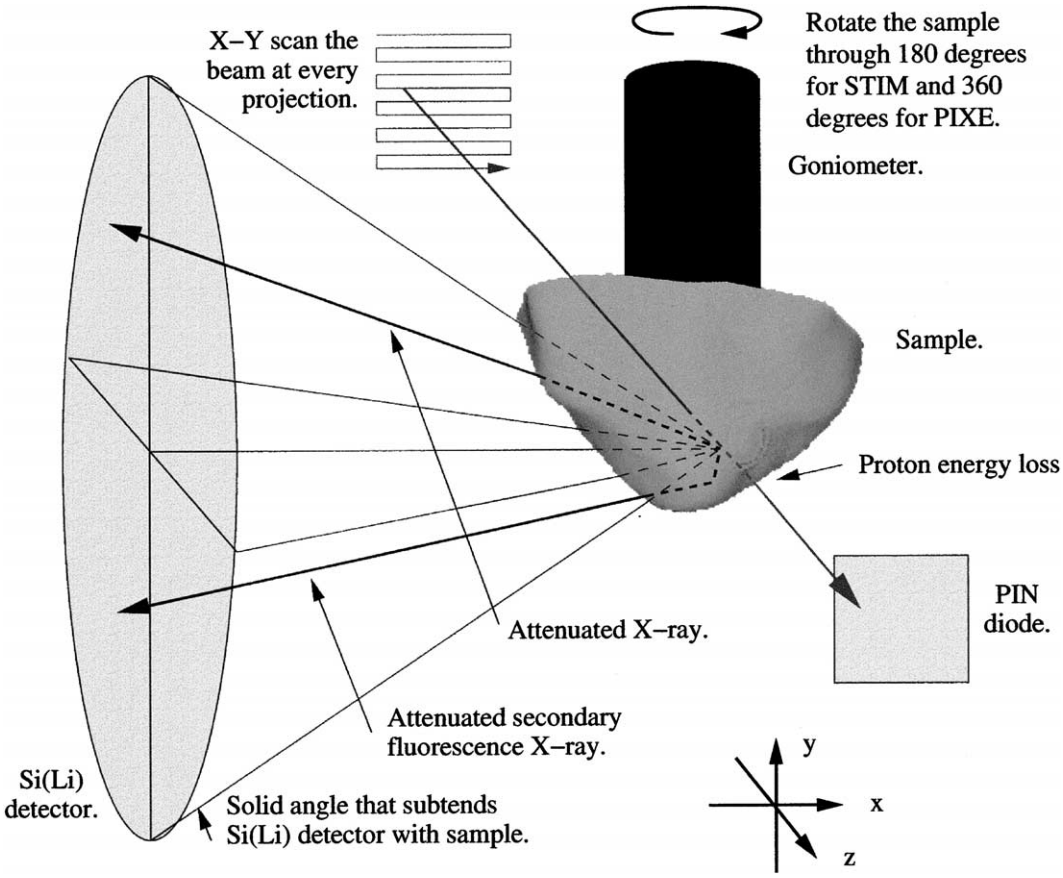

Fig. 1. Diagram of the IMT experiment.

and was acquired at an average rate of 5.6k counts per second. This is compared to the spatial resolution of 0.25 μm for the STIM data, which was acquired at an average rate of 9.9k counts per second.

2. Automation of experiment

There are many features required by a DAS to optimise the quality and throughput of collecting data for a tomography experiment.

The features of the STIM experiment are: data rates above 40k events per second, a beam blanking signal, data triggering for the scan dwell, a raster scan and a signal to block the ion beam when data are not being collected.

The high data rate allows for reduced experiment times by increasing the current of the STIM beam. A beam blanking signal deflects the beam off the sample when the DAS is busy digitising the energy of the detected proton. This reduces pile-up and entices the DAS to measure the energy of only one proton at a time, resulting in more accurate energy data. Data triggering allows the scan to dwell at each pixel until a preset number of protons, usually seven, have been detected. To calculate the energy loss at each pixel, the median energy of the detected protons is calculated. A raster scan allows for two-dimensional maps to be generated. The purpose of blocking the proton beam when data are not being collected is to prevent unnecessary damage to the p–i–n diode. This allows for more projections to be collected without the need to reposition the p–i–n diode.

The features of the PIXE experiment are: data rates above 33k events per second, a beam blanking signal, smart (data) triggering for the scan dwell, measuring charge so that charge-normalised maps can be generated and at least a raster scan.

The high data rate allows for reduced experiment time by increasing the current of the PIXE beam and/or by increasing the solid angle that the X-ray detector subtends with the sample. This implies that the spatial resolution of PIXE data can be optimised, whilst maintaining data acquisition rates, by simultaneously reducing the beam current and increasing the solid angle. A beam blanking signal deflects the beam off the sample when the DAS is busy digitising the energy of any X-rays that are generated. This reduces pile-up and entices the DAS to measure the energy of only one X-ray at a time. Smart (data) triggering is a mode that allows a preset number of X-rays to be collected at each pixel, but is capable of skipping the pixel if no X-rays are being collected, as in the case when the proton beam is not striking the sample. This helps to reduce experiment times because the scan does not waste time by dwelling at pixels where there is no sample, as in the case of charge triggering. However, by collecting a fixed number of X-rays at each pixel, the accuracy of the X-ray yield at each pixel can be controlled. To collect a fixed number of X-rays at each pixel implies the amount of incident charge varies from pixel to pixel. To generate X-ray maps that are spatially normalised with respect to charge, the incident charge at each pixel must be collected. The incident charge is measured with a deep-well Faraday cup, situated behind the sample. Note that, for such a mode to be practical, a very sensitive charge-to-frequency converter is required. Another benefit of beam blanking is that any effects of dead time are eradicated because the charge is gated and so the X-ray yield is purely due to the measured incident charge. So, the X-ray yield only needs to be corrected for charge. A raster scan is required to generate the two-dimensional X-ray maps. However, a dithering raster scan system was also devised so that a rectangular region can be scanned without any adjacent pixels being irradiated [1]. This is used to reduce damage to samples that are prone to thermal damage.

A computer program, called "mpcat", is used to automatically collect all of the projections required for a tomography experiment. The program starts and stops the data acquisition and rotates the sample after each projection. In the event that the sample moves outside of the "field-of-view" of the scan, an "edge detection" algorithm automatically halts the experiment and informs the user that the experiment requires attention. The user then re-adjusts the position of the sample and then informs the program to resume the experiment.

3. Reconstruction technique

The technique used to reconstruct STIM and PIXE tomography data is the DISRA [2,3]. DISRA is our extension of the image space reconstruction algorithm (ISRA) [16]. The main feature of DISRA is that the density of inhomogeneous samples can be reconstructed from experiments in which complex physical phenomena occur when a probe interacts with the sample. This is accomplished whilst also retaining accurate density information at every voxel.

Fig. 2 shows a diagram of the steps required for the DISRA technique. The DISRA technique is iterative and, at every iteration, the approximated density, called the tomogram, of the physical sample is improved. To start the iteration, an initial estimate of the sample's density is calculated by scaling the reference reconstruction into an acceptable tomogram.

The iterative improvements to the tomogram are achieved by performing two steps. The first step is to calculate a simulated sinogram by using the tomogram in a simulation of the tomographic experiment. The simulation requires a model of the experiment incorporating as many significant physical phenomena as possible. The more precise the simulation, the better the results. However, a compromise between accuracy and computation time is required. The second step involves comparing the reference reconstruction with the simulation reconstruction to provide correction factors for the tomogram. The correction factors are simply the reference reconstruction divided by the simulation reconstruction at every voxel.

The second step is the most significant aspect of the DISRA technique. It enables the simulation reconstruction to converge to the reference reconstruction. If the simulation is a sufficiently accurate model of the processes that occur during the experiment, then when the experimental and simulated sinograms are similar, the tomogram is an accurate representation of the sample's physical characteristics.

The simulation of the STIM and PIXE experiments would involve the modelling of numerous physical phenomena, as shown in Fig. 1. To make computation time practical, only a few significant phenomena are incorporated.

The energy loss due to the stopping power of an ion beam is implemented. Since elemental composition information is required, the accuracy of the mass density solutions are critically dependent on the accuracy of the composition information. This information is obtained from the PIXE data. However, low-Z elements cannot be detected with PIXE analysis. This will always lead to problems when calculating the mass density of a sample but can be minimised by including appropriate a priori elemental composition information. A beam broadening model for an inhomogeneous sample is complicated and is excluded from the model because it would be too computationally expensive.

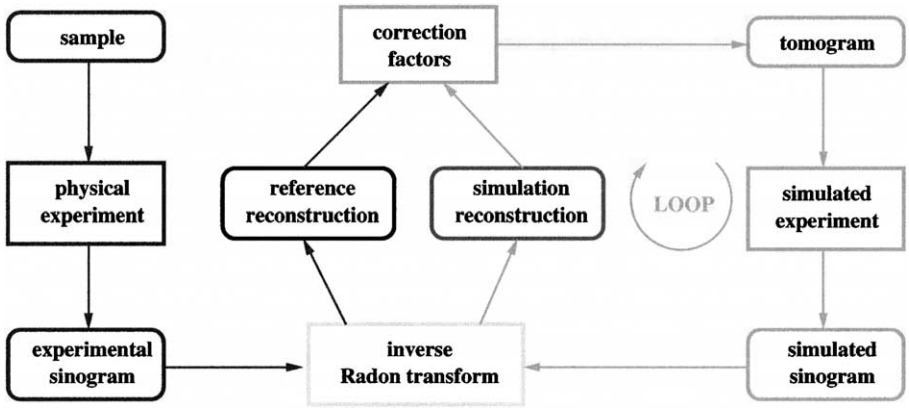

Fig. 2. Flowchart of the DISRA technique.

Characteristic X-rays are used to identify what elements are present in the sample. To model the yield of these X-rays, the X-ray production cross-section is incorporated into the model. The accuracy of the yield is maintained by including the energy loss dependence of the proton's energy as it traverses the sample. Each element is identified with one K-shell or L-shell X-ray that has the largest yield. This allows the X-rays from each element to be identified by only one X-ray, which substantially reduces the number of calculations that are performed in the simulation.

Since the majority of X-rays are produced from deep inside the sample, the attenuation of the X-ray yield as they traverse the sample to the X-ray detector can be substantial. The reduction of X-ray yield varies significantly with the path of the X-ray to the detector. This requires accurate mass density information, which is obtained from STIM data. Since a large solid angle is used, the effect on the X-ray yield for many different paths needs to be incorporated into the model. This is implemented as a cone geometry between the sample and the X-ray detector. This is computationally expensive but is essential to ensure an accurate simulation of X-ray yield.

X-ray secondary fluorescence should also be included in the model. However, this would be computationally expensive, as it requires many X-ray paths to be simulated throughout the tomogram. However, by evaluating the elements that are present in the PIXE data, it is possible to ascertain if the elements present do significantly interact via secondary fluorescence. Under such circumstances the model should include X-ray secondary fluorescence.

Note that the quantitative accuracy of the mass density and elemental concentration tomograms will always be limited by the numerical precision of the expressions that are used to simulate these physical phenomena. So, excluding the phenomena of beam broadening and secondary fluorescence will always reduce the precision of any tomogram. The main effect on the tomogram would probably be incorrect localisation of mass density and elemental concentration values that would manifest themselves as incorrect structural information.

4. Test using a "standard" sample

A test sample was made by selecting some powder chemicals and cutting one "ladder" from a 2000 mesh copper grid. These were embedded in Araldite. The powder chemicals are lead fluoride (PbF_2), vanadium (V) oxide (V_2O_5), copper (II) oxide (CuO), lead (II) chloride ($PbCl_2$) and potassium chloride (KCl). There are a few reasons why these chemicals were chosen. The X-ray peaks do not overlap so they are easy to identify and their yield can be accurately measured. Also, a few aspects of the reconstruction code are tested: Can the technique calculate the concentration of an element that has no variation between different regions of the sample (e.g. the V in V_2O_5 and the K in KCl)? Can the technique calculate the concentration of an element that has different concentrations in different parts of the sample (e.g. the Cu in Cu (grid) and CuO, the Pb in $PbCl_2$ and PbF_2 and the Cl in KCl and $PbCl_2$)? Can the technique calculate the elemental concentration and mass density of regions in which the compound cannot be completely detected by PIXE (e.g. CuO, V_2O_5 and PbF_2)?

Anyway, the data were collected to have a dimension of $200 \times 200 \times 250$ pixels of a dimension of $50 \times 50 \times 62.5$ μm^3. The STIM data consist of 312 projections through 180° with a spatial resolution of 0.25 μm and the PIXE data consist of 152 projections through 360° with a spatial resolution of 0.5 μm. The STIM data took 5 h to collect and consisted of 1 GB of data. The PIXE data took 35 h to collect and consisted of 4 GB of data. The resolution of the charge information for the PIXE data was 10 fC per pulse. The elemental maps of the PIXE data were extracted and charge-normalised. The reconstruction only took eight iterations.

Fig. 3 shows the reconstruction of one slice from the tomogram and Table 1 shows the average reconstructed mass density and elemental weight fractions of the specified regions. To ensure that the weight fractions add to one at each voxel, the a priori data of Araldite were used. As will be discussed, this does cause problems for the results associated with CuO, V_2O_5 and PbF_2.

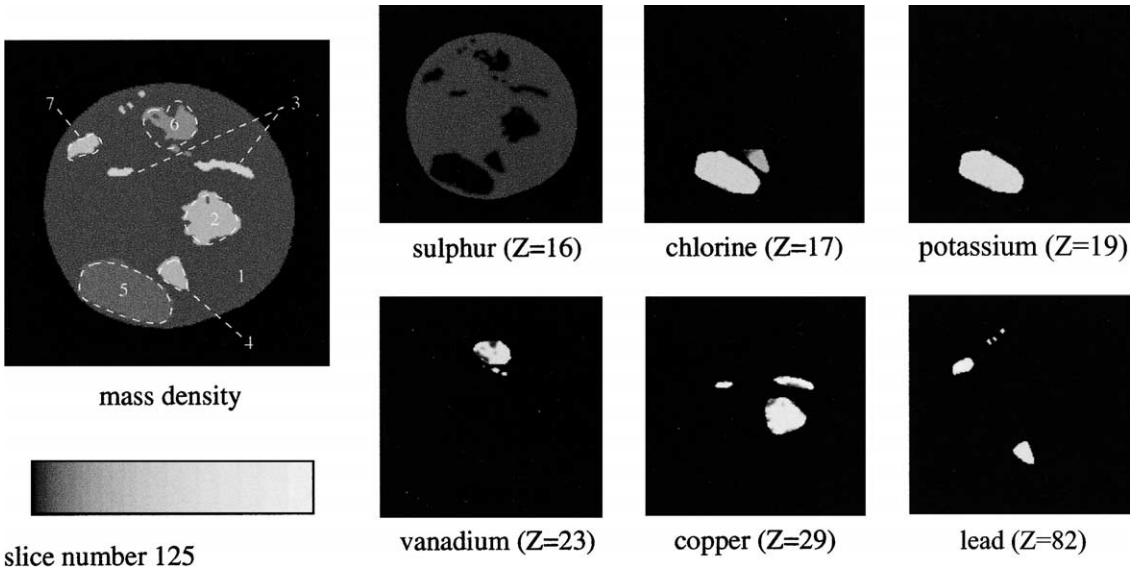

Fig. 3. Some results from slice number 125 (black and white copy of colour original, see text).

Table 1
Some results from slice number 125

Region	Composition	Known mass density (g cm^{-3})	Average reconstructed mass density (g cm^{-3})	Known weight fractions	Average reconstructed weight fractions
1	Araldite	1.1	1.15 ± 0.50	S: 0.047	S: 0.045 ± 0.006
2	CuO	6.4	5.71 ± 1.24	Cu: 0.80	Cu: 0.80 ± 0.16
3	Cu (grid)	9.0	8.73 ± 1.22	Cu: 1.00	Cu: 0.97 ± 0.08
4	$PbCl_2$	5.8	5.66 ± 0.11	Cl: 0.255 Pb: 0.745	Cl: 0.248 ± 0.009 Pb: 0.738 ± 0.006
5	KCl	2.0	1.97 ± 0.12	Cl: 0.48 K: 0.52	Cl: 0.46 ± 0.06 K: 0.51 ± 0.07
6	V_2O_5	3.4	2.82 ± 0.67	V: 0.56	V: 0.52 ± 0.18
7	PbF_2	8.2	5.75 ± 1.84	Pb: 0.84	Pb: 0.78 ± 0.30

The average mass density for the Araldite, Cu (grid), $PbCl_2$ and KCl regions have been accurately calculated. This is mainly due to the fact that all of the elements of these regions were detected by PIXE and the weight fractions are calculated accurately. Even though Araldite also consists of H, C and O, these were provided as a priori data and were used to re-normalise, if required, the weight fractions at each voxel to one.

However, the average mass density for the CuO, V_2O_5 and PbF_2 regions have not been accurately calculated. The elemental compositions of these regions have not been fully calculated and the a priori data used have had a significant effect on the mass density calculations. However, the calculation of the weight fractions of the detected elements are reasonably accurate, except for the PbF_2 region. This may be due to the fact that the X-ray production cross sections for L X-rays are not as accurate as for the K X-rays.

Note that even though some regions cannot be characterised properly, they do not have a perceivable effect on the accuracy of the well-characterised regions.

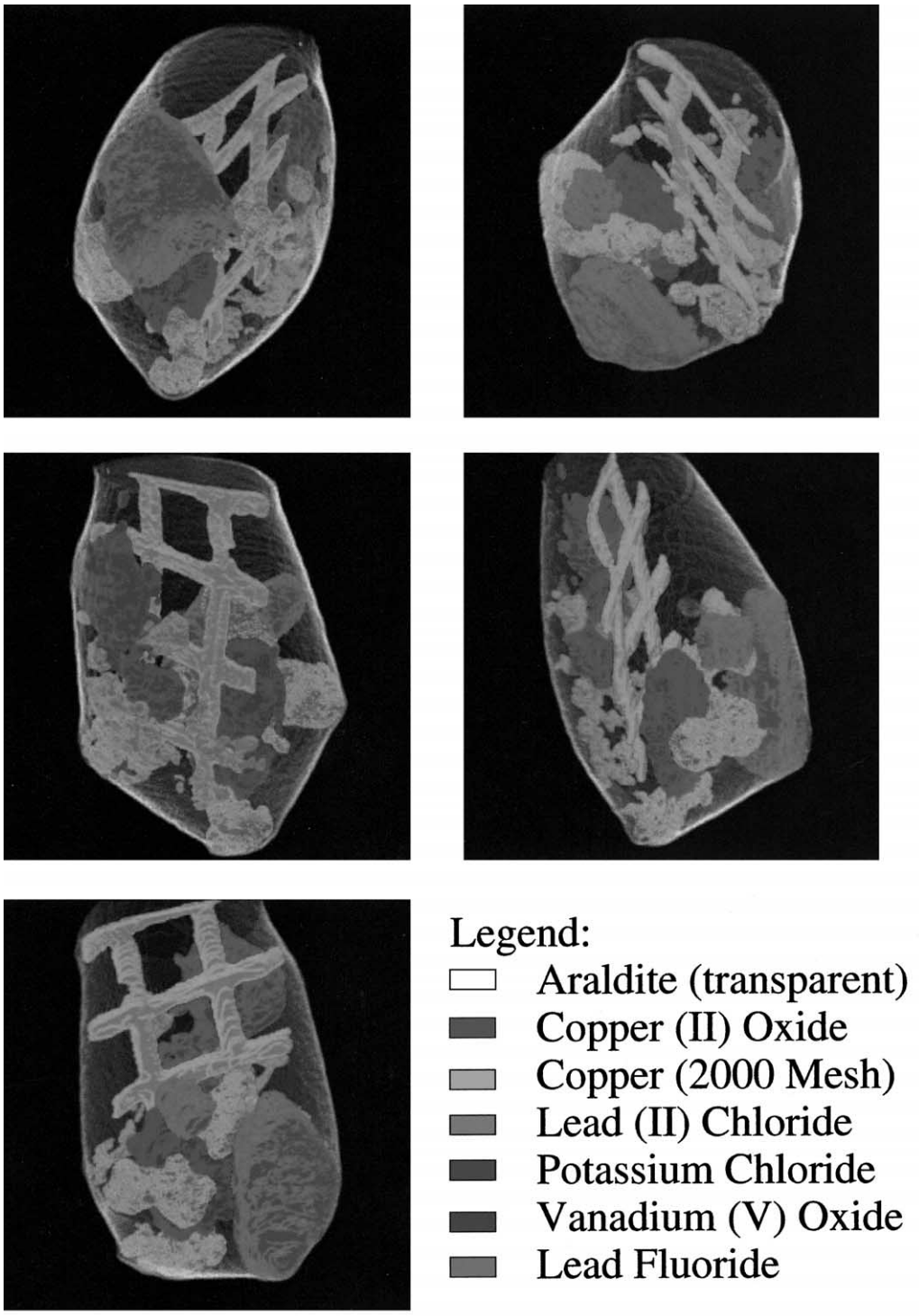

Fig. 4. Some renderings of the tomogram (black and white copy of colour original, see text).

One aspect of the reconstructed data is that the regions have a very smooth distribution of values. This is an important capability of the DISRA technique. Unfortunately, no structural information can be obtained from the data in Fig. 3. So, in Fig. 4, some renderings of the entire data set are shown. Note the structural quality of the 2000 mesh copper grid. Colour images of Figs. 3 and 4 can be obtained from http://www.ph.unimelb.edu.au/marc/nimb15251.html.

5. Conclusion

The experimental setup for IMT has been optimised to collect accurate STIM and PIXE data with large data acquisition rates. Even though these experiments still take several hours to complete, the total automation of these experiments does help alleviate the physical and mental burden of the user.

The three-dimensional distributions of the mass density and elemental concentration of micro-samples can be determined accurately. However, the inability of PIXE to detect low-Z elements has a significant effect on the accuracy of the calculated mass density in regions where low-Z elements are located. The only way to improve this is to allocate more accurate a priori data to these regions. This may seem contradictory to our initial motivation, but it does allow for a mechanism to generate three-dimensional distributions of these a priori compounds.

References

[1] A. Sakellariou, G.R. Moloney, D.N. Jamieson, Nucl. Instr. and Meth. B 181 (2001) 116.
[2] A. Sakellariou, M. Cholewa, A. Saint, G.J.F. Legge, Meas. Sci. Technol. 8 (1997) 746.
[3] A. Sakellariou, M. Cholewa, A. Saint, G.J.F. Legge, Nucl. Instr. and Meth. B 130 (1997) 253.
[4] A.E. Pontau, A.J. Antolak, D.H. Morse, A.A. Ver Berkmoes, J.M. Brase, D.W. Heikkinen, H.E. Martz, I.D. Proctor, Nucl. Instr. and Meth. B 40–41 (1989) 646.
[5] A.E. Pontau, A.J. Antolak, D.H. Morse, Nucl. Instr. and Meth. B 45 (1990) 503.
[6] A.E. Pontau, A.J. Antolak, D.H. Morse, D.L. Weirup, Nucl. Instr. and Meth. B 54 (1991) 383.
[7] G. Bench, K.A. Nugent, M. Cholewa, A. Saint, G.J.F. Legge, Nucl. Instr. and Meth. B 54 (1991) 390.
[8] G. Bench, A. Saint, M. Cholewa, G.J.F. Legge, Nucl. Instr. and Meth. B 68 (1992) 481.
[9] R.M.S. Schofield, H.W. Lefevre, Nucl. Instr. and Meth. B 72 (1992) 104.
[10] A. Saint, M. Cholewa, G.J.F. Legge, Nucl. Instr. and Meth. B 75 (1993) 504.
[11] R.M.S. Schofield, H.W. Lefevre, Nucl. Instr. and Meth. B 77 (1993) 217.
[12] A.J. Antolak, G.S. Bench, Nucl. Instr. and Meth. B 88 (1994) 297.
[13] A.J. Antolak, G.S. Bench, A.E. Pontau, D.H. Morse, D.W. Heikkinen, D.L. Weirup, Nucl. Instr. and Meth. A 353 (1994) 568.
[14] R.M.S. Schofield, Nucl. Instr. and Meth. B 104 (1995) 212.
[15] S.C. Liew, I. Orlic, S.M. Tang, Nucl. Instr. and Meth. B 104 (1995) 222.
[16] M.E. Daube-Witherspoon, G. Muehllehner, IEEE Trans. Med. Imag. 5 (1986) 61.